Research Article Vol. 32, No. 4 / 12 Feb 2024 / Optics Express 5252
Optics EXPRESS

Measured optical losses of Sc doped AlN waveguides

B. Friedman,[1,*] S. Barth,[2] T. Schreiber,[2] H. Bartzsch,[2] J. Bain,[1] and G. Piazza[1]

[1]Electrical and Computer Engineering, Carnegie Mellon University, 5000 Forbes Ave., Pittsburgh, PA 15213, USA
[2]Fraunhofer Institute for Organic Electronics, Electron Beam and Plasma Technology FEP, 01277 Dresden, Germany
[*]BenFriedman@cmu.edu

Abstract: Although Sc doped AlN (ScAlN) has been used extensively in micro-electro-mechanical systems (MEMS) devices and more recently in optical devices, there have not been thorough studies of its intrinsic optical losses. Here we explore the optical losses of the $Sc_{0.30}Al_{0.70}N$ waveguide system by observing racetrack resonator waveguide quality factors. Using a partial physical etch, we fabricate waveguides and extract propagation losses as low as 1.6 ± 0.3 dB/cm at wavelengths around 1550 nm, mostly dominated by intrinsic material absorption from the $Sc_{0.30}Al_{0.70}N$ thin film layer. The highest quality factor of the resonators was greater than 87,000. The propagation loss value is lower than any value previously published and shows that this material can be broadly used in optical modulators without significant loss.

1. Introduction

The non-centrosymmetric structure of aluminum nitride (AlN) gives rise to its Pockels effect which, in combination with AlN's low loss and high transparency window, allows for electro-optic signal processing with speeds up to 4.5 Gb/s and energy consumption as low as 10 fJ/bit from visible to mid-infrared wavelengths [1,2]. While the fabrication of AlN electro-optic modulators is compatible with Si backend integration, the devices have low modulation efficiency, requiring voltages too high for CMOS operation [3]. Doping (AlN) with scandium (Sc) has been used to increase (up to 5x) AlN piezoelectricity [4] while maintaining the CMOS compatibility using magnetron sputtering techniques [5]. Due to its increased piezoelectricity, ScAlN films have been demonstrated to achieve high performance surface acoustic waves (SAWs) [4]. AlN photonic platforms have utilized SAWs in order to achieve acousto-optic modulation of photons with wave frequencies at 10 GHz [6] and 12 GHz [7]. Despite the benefits, very little research has explored the effect of Sc doping on the optical properties of AlN. Due to the interconnected nature of piezoelectricity and optical properties, we expect to see similarly drastic improvements in electro-optic and acousto-optic characteristics as a result of the Sc doping. Recently, there have been promising demonstrations of second-order nonlinearities twice as strong as in lithium niobate in $Sc_{0.36}Al_{0.64}N$, but the propagation losses at telecommunication wavelengths from these waveguides were very significant (> 15 dB/cm) [8]. Ellipsometry measurements have estimated the ScAlN material bandgap and optical constants as a function of Sc content through parametric oscillator model fitting. These findings indicate that the absorptive losses at telecommunication wavelengths should be very low due to these wavelengths being at the far end of their fit's Urbach tail [9]. To date, the ScAlN waveguide propagation losses around 1550 nm wavelength have been reported to range from 8.2 dB/cm to over 17 dB/cm [8,10,11] and can be summarized in Table 1. Although higher Sc content is expected to increase material absorption [8,9], the current reported measurements do not strictly follow that trend due to the losses being dominated by sources other than material absorption.

#511606 https://doi.org/10.1364/OE.511606
Journal © 2024 Received 8 Nov 2023; revised 22 Dec 2023; accepted 3 Jan 2024; published 30 Jan 2024

Optics EXPRESS

Table 1. Comparisons of other works that characterize ScAlN waveguide losses.[a]

Sc Content	Measurement Method	Loss [dB/cm]	Main Loss Source	Reference
20%	Wafer Prism Coupling	8.2	Grain Structure	[8]
36%	Wafer Prism Coupling	17.2	Grain Structure	[8]
15%	80 μm Ring Resonator	9±2	Fabrication	[10]
20%	100 μm Ring Resonator	>17 (est.)	-	[11]
35%	Racetrack Resonator	1.6±0.3	Material Absorption	This work

[a]No other study has attributed most of the propagation loss to material absorption (Ref. [11] loss value is estimated from the reported resonator Q=5000).

In this work, we investigated propagation losses in 30% doped AlN ($Sc_{0.30}Al_{0.70}N$). The propagation losses of $Sc_{0.30}Al_{0.70}N$ rib waveguides on SiO_2 cladding were extracted from racetrack resonators' intrinsic quality factors. The fabrication process, including the partial waveguide etch, were designed to moderate the losses due to fabrication imperfections. Various racetrack lengths were considered in order to accurately extract propagation losses in the straight portions of the waveguides. Furthermore, multiple $Sc_{0.30}Al_{0.70}N$ film thicknesses were considered in order to better identify the role of the core material absorption in the overall device losses. In this report, we report the lowest propagation losses recorded as low as 1.6 ± 0.3 dB/cm for relatively high (30%) concentrations of Sc. We further report, for the first time, that the loss value is dominated by material absorption.

2. Fabrication

2.1. $Sc_{0.30}Al_{0.70}N$ deposition and wafer stack preparation

The $Sc_{0.30}Al_{0.70}N$ films were deposited by reactive pulse magnetron sputtering using the double ring magnetron DRM 400 of Fraunhofer FEP [12]. The DRM 400 consists of two concentric targets, whose discharges overlap to deposit homogeneously on 200 mm diameter area. Pulse powering in unipolar-bipolar hybrid pulse mode was used to adjust plasma properties [12]. A closed-loop reactive gas control was applied to stabilize the process in the transition mode [13]. ScAl Alloy targets with 30 at.% Sc and purity 3N5 were used to deposit the ScAlN films. Argon (5N) and nitrogen (5N) were used as inert and reactive gas, respectively. Substrate temperature at the beginning of the deposition was around 200°C. The base pressure of the coating chamber was 2×10^{-7} mbar.

The coatings were done on 4" Si-Wafers with 5 µm SiO_2. The wafers were positioned off-center of DRM axis to cover the whole 200 mm diameter area of coating. Prior to the deposition of ScAlN, rf plasma etching was used to remove surface contaminations from the wafers. The thicknesses of the deposited ScAlN films were 150 nm, 250 nm and 300 nm. The deposition rate was 2.0 nm/s.

Film structure was investigated by XRD using Bruker D8 Discover diffractometer equipped with a Göbel mirror for Cu-Ka parallel beam geometry and a 1D LynxEyeTM XET semiconductor detector (Bruker AXS, Karlsruhe, Germany). The films were characterized using XRD θ-2θ scan in 1D detector mode for investigating the lattice parameters of the wurtzite structure. The ScAlN (002) rocking curve in 0D detector mode was used to investigate film quality of crystallographic orientation. Only the (002) and (004) Peaks of ScAlN Wurtzite structure, besides the Si substrate peaks, were visible in θ-2θ scan (see Fig. 1). The Full-width-at-half-maximum (FWHM) of ScAlN (002) rocking curve was 2.9° for 250 nm film thickness.

In preparation for the fabrication of the optical devices, a bi-layer hard mask of 125 nm PECVD SiO_2, and 25 nm of Cr was deposited on top of the investigated wafer stack.

Optics EXPRESS

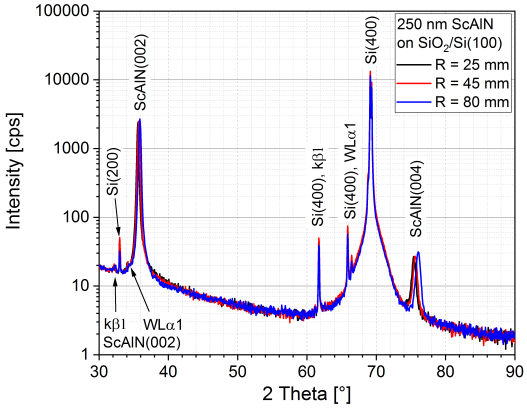

Fig. 1. XRD θ-2θ scan of 250 nm ScAlN on SiO2/Si(100) substrate at 3 radial positions R in 200 mm diameter coating area, only the substrate and ScAlN (002) / (004) peaks visible, measured at different deposition radii.

2.2. Optical device

The wafer stack was then fabricated into rib waveguide racetrack resonators for testing. The rib waveguides were 2.5 μm wide and had 5 μm trenches isolating them from the unetched regions of the film into which the optical mode would otherwise leak. The racetrack resonators varied in racetrack length from 100 μm to 2000 μm while the bend radius remained constant at 200 μm. The waveguides pumping the resonators and the resonators themselves had the same rib waveguide structure. The resonators, the pumping waveguides, and the grating couplers were all defined on the same layer. The pulley coupling technique was used to couple the resonator and waveguide with a coverage angle of 25°and coupling gaps ranging between 50 nm to 200 nm in order to easily identify resonances over a wide range of propagation losses. Images of various fabricated devices are shown in Fig. 3

Traditionally, AlN dry chemical etches using Cl-based recipes can achieve etches with smooth, 80-90°sidewalls quickly. With the addition of Sc, those processes become drastically worse due to the low volatility of $ScCl_3$ [14]. Wet etching is another option for etching ScAlN, although the best wet etchants are 25 weight-% TMAH, which is highly toxic, or NaOH or KOH, which are known to produce alkali metal contamination [15]. Ultimately, we chose a physical partial etch of the core layer which resulted in acceptable processing times while, according to simulation for each film thickness, consistently allows for sufficient grating coupler efficiency and confinement of optical modes for our film thickness range. Additionally, the relatively short etch depth minimizes the interactions of the waveguide modes with rough sidewalls that are expected from a physical etch.

The process flow used to define the optical structures from the material stack is shown schematically in Fig. 2. The pattern was defined using electron beam lithography and AR-P 6200.18 resist. The resist was removed after using it as a mask to transfer the pattern to the Cr layer during a ICP RIE Cl_2 etch at 10mT with 600W ICP power. Next, the SiO_2 was etched down to the $Sc_{0.30}Al_{0.70}N$ layer using CHF_3 and O_2 in a RIE tool at 100 mT, 320 V bias voltage, and 100 W power while the Cr layer acted as a hard-mask. Finally, the thin layer of Cr and the thicker SiO_2 acted as a hard-mask during an Ar based ion-mill of the $Sc_{0.30}Al_{0.70}N$ with 500 V beam voltage, 250 mA beam current, and 100 V accelerator voltage. Under the ion mill conditions, we etched to the target 100 nm depth in 12 minutes for all devices, resulting in an etch rate of about 1.36 Å/s. The Cr is assumed to have been removed by the physical etching. To avoid introducing the unknown optical properties of the PECVD SiO_2 to the devices, the SiO_2 was

Optics EXPRESS

removed through a 10:1 HF wet etch. The partial etch of the core material prohibits the HF from attacking the lower SiO_2 cladding layer. Finally, a post process RCA 1 cleaning was performed to remove any impurities on the surface.

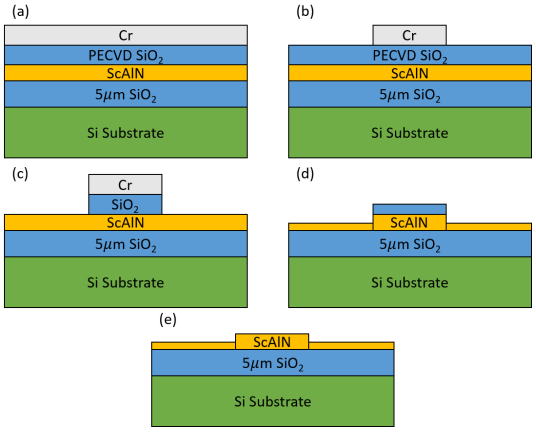

Fig. 2. Process Flow. (a) Device stack, (b) Cr etch in Cl_2, (c) SiO_2 etch in CHF_3 and O_2, utilizing extremely high selectivity of the SiO_2 to Cr, (d) $Sc_{0.30}Al_{0.70}N$ ion-mill etch, etching the $Sc_{0.30}Al_{0.70}$ and hard mask at an estimated 1:1 rate. (e) Wet etch SiO_2 in HF, selectively attacking the SiO_2.

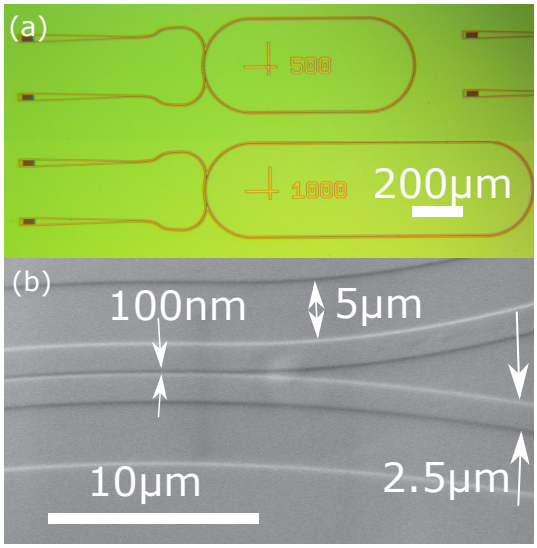

Fig. 3. (a) Optical image of two devices with racetrack lengths of 500 μm and 1mm and bend radii of 200 μm. (b) SEM image of the pulley coupling region between the resonator and pumping waveguide with a 100 nm gap. Both paths consist of a 2.5 μm waveguide with a 5 μm trench on either side. The slight discoloration is due to charging effects.

3. Experiment

The racetrack resonators were tested by observing the transmission of laser power through the on-chip waveguides and patterned gratings. A Santec TSL-510 tunable laser source supplied

Optics EXPRESS

input power at 10 mW through input grating couplers and a V-groove assembly (VGA) with a measured 8 dB loss per grating. The transmission was collected at the output grating couplers through the same VGA and the transmitted power was measured from a photodetector. The low power resulted in minimal heating of the device, avoiding any nonlinearities in the resonator response. The tunable laser was used to sweep the input wavelength around 1550 nm through the waveguide-resonator pair with pm resolution and the transmission was recorded. Although the waveguide supports multiple modes, the first order TE mode resonance was identified by choosing the mode with the highest group index and isolating it by moving to an input wavelength where the other modes' resonances did not overlap. In order to characterize the resonant behavior of the system, the normalized transmission around one resonant wavelength was fit to the curve following a modified Lorentzian equation:

$$T = 1 - \frac{\frac{1}{Q_i}\frac{1}{Q_c}\lambda_r^2}{(\lambda - \lambda_r)^2 + \frac{\lambda^2}{4}\left(\frac{1}{Q_i} + \frac{1}{Q_c}\right)^2} \tag{1}$$

where T is the normalized transmission, λ_r is the resonant wavelength, and Q_i and Q_c are the intrinsic and coupling quality factors, respectively. With respect to the curve fitting, Q_i and Q_c are interchangeable. Therefore, if the waveguide and resonator were not critically coupled ($Q_i \neq Q_c$), the fit alone would result in two possible values for Q_i. Due to the nature of the racetrack resonators, Q_i increases inversely with the racetrack length while Q_c increases linearly. Using these trends across many racetrack lengths, we could confidently identify both parameters of the fit.

The loaded Q (Q_L), sometimes referred to as just Q, is often cited as it represents the lowest possible value of the resonator's intrinsic quality factor. Q_L is directly measured from the full width half max of the transmission around resonance. It can be decomposed into its components as:

$$\frac{1}{Q_L} = \frac{1}{Q_i} + \frac{1}{Q_c} \tag{2}$$

Furthermore, the free spectral range (FSR) was recorded as the distance between resonant wavelengths. It was used to calculate the group index of the specified mode:

$$n_g = \frac{\lambda_r^2}{\Delta\lambda L} \tag{3}$$

where n_g is the group index, $\Delta\lambda$ is the FSR, and L is the total path length of the resonator. The group index and the intrinsic quality factor were both used to calculate the propagation power decay coefficient α (units m^{-1}):

$$\alpha = \frac{n_g \pi}{Q_i \lambda} \tag{4}$$

In this report, the propagation power decay is represented in terms of dB/cm through a unit conversion from α. These propagation losses per unit length represents the total power losses divided by the entire path lengths of the resonators. These are the values that are directly measured, while the subsequent analysis of these values extracts the losses in the straight portion of their racetrack resonators.

The propagation losses in the bends of the resonators are different from the propagation losses in the straight racetrack portions due to dissimilar interactions with the sidewalls and radiation into the substrate/cladding. For each device, the contribution of the bending and straight portions of the waveguide toward the total average propagation loss is a weighted average of the two propagation losses in each region. The weights are determined from the device geometry by the proportion of the total resonator path length that each portion represents. Also present

Optics EXPRESS

in the average propagation loss measurements is a contribution from four small point losses originating from the mismatch of the modes at the transition from bending to straight portions of the waveguide. These contributions are summarized in Eq. (5) as a linear function for $\eta>0$:

$$\begin{aligned}\frac{Loss_{total}}{Length_{total}} &= \frac{L_s + L_b + L_x}{r + b} \\ &= \left(\frac{L_s}{r} - \frac{L_b}{b} - \frac{L_x}{b}\right) \times \eta + \frac{L_b}{b} + \frac{L_x}{b}\end{aligned} \tag{5}$$

where L_s, L_b, L_x are the total losses in dB in the straight region, the bending region, and the transitions, respectively; and r and b are the total length in cm of the racetrack and bend, respectively. η is the fraction of total resonator path length that is straight, calculated by $\eta = r/(r + b) = r/L$.

4. Results

Using the above procedures, the average propagation losses over the entire resonator path length of the first order TE modes for all devices were extracted. The corresponding TE mode group indices were consistent within each device with the same $Sc_{0.30}Al_{0.70}N$ film thickness: 1.83, 2.14, 2.23 for the 150 nm, 250 nm, and 300 nm film thickness, respectively.

For each film thickness, the measured average propagation losses fit linearly to the fraction of total resonator path length that is straight (η). Because the bends for each device have the same path length, the linear fit represents the same function from Eq. (5). For each thickness, a weighted linear fit was performed, using the quality of the modified Lorentzian fit as a weight for each data point considered. By extrapolating the resulting fit to a resonator that is 100% straight ($\eta = 1$), we extracted the loss per unit length of the straight portion of the waveguide. The combined contribution of the propagation loss in the bend and the transition losses to the measured average losses are also represented in the fit as the extrapolation to 0% straight ($\eta = 0$). Although we cannot directly separate the individual contributions from the combination, simulations of the overlap integrals between the straight propagating mode and a bending mode for each film thickness, along with the known path length of the bends, give an estimate of the magnitude of the transition loss' contribution.

The measured average losses per unit length for all devices fabricated from the three film thicknesses, and the resulting linear fits, are shown in Fig. 4. For these devices, the extracted straight propagation losses and extracted combined contribution of other losses, along with the simulated contribution of transition losses, are reported in Table 2. The measured values in Fig. 4 specify the average propagation losses of our devices which consist of both material losses and losses due to fabrication imperfections. In order to better assess the intrinsic material losses, which should be consistent between devices, we performed the same analysis as we did with all the data but only considered the devices which had the lowest average propagation losses for each film thickness and racetrack length. The propagation losses from this analysis better approximate the propagation losses due to material losses because the contribution from fabrication imperfections is lowest in these devices. The resulting linear fits are shown in Fig. 5, and the extracted propagation losses are also reported in Table 2.

The device with the best performance had a film thickness of 150 nm and had the longest racetrack length (2 mm). The device had a Q > 87k corresponding to a total average propagation loss of 2.26 ± 0.06 dB/cm from considering both the bending and straight portions of the resonator. A demonstration of the resonant behavior and the corresponding fit is shown in Fig. 6. The linear extrapolations predict that a device with lower average propagation loss than the one referenced could be fabricated by increasing the racetrack length, thus bringing the average propagation loss closer to that of the straight portion. This data point also serves as a directly measured upper

Optics EXPRESS

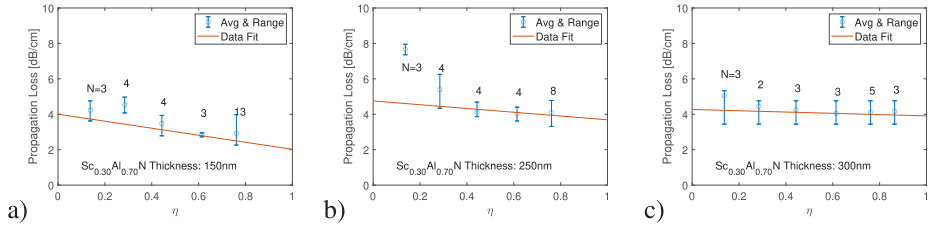

Fig. 4. Average propagation loss values and weighted linear fits over multiple racetrack lengths for all devices fabricated using (a) 150 nm film considering 27 devices, (b) 250 nm film considering 23 devices, (c) 300 nm film considering 19 devices. The data points and error bars represent the simple mean and range of all extracted loss values for each fraction of total resonator path length that is straight (η) while the fit was found by considering the weighted loss values. N indicates the number of samples at each η value.

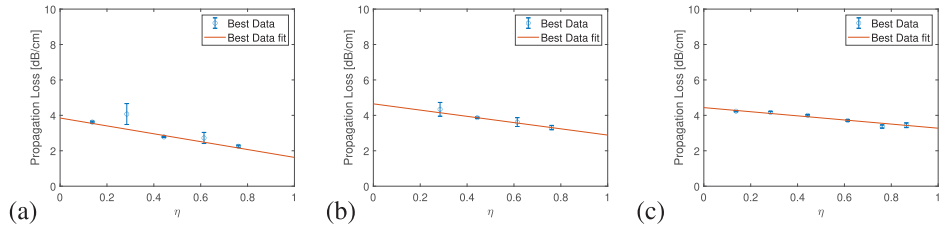

Fig. 5. Average propagation loss values and linear fits over multiple racetrack lengths for best performing devices fabricated using (a) 150 nm film, (b) 250 nm film, (c) 300 nm film. The data points represent the lowest extracted average propagation loss value for each fraction of total resonator path length that is straight (η). The error bars represent the inverse square root of the weights used in the fit, calculated by the quality of the modified Lorentzian fit.

Table 2. Propagation losses in the straight portion of waveguide and combined other contributions that were extracted from the from the linear fit.[a]

Thickness $Sc_{0.30}Al_{0.70}N$ [nm]	L_s/r (All Data) [dB/cm]	$L_b/b + L_x/b$ (All Data) [dB/cm]	L_s/r (Best Points) [dB/cm]	$L_b/b + L_x/b$ (Best Points) [dB/cm]	L_x/b (Simulated) [dB/cm]
150	2.0 ± 0.5	4.0 ± 0.2	1.6 ± 0.3	3.85 ± 0.15	0.28
250	3.7 ± 1.0	4.8 ± 0.5	2.9 ± 0.2	4.65 ± 0.09	0.41
300	3.9 ± 0.4	4.27 ± 0.17	3.27 ± 0.19	4.43 ± 0.07	0.56

[a]The uncertainties derive from the uncertainties in the weighted linear fits. The contribution of losses from the transitions were estimated from an overlap integral and the known resonator geometry.

bound for propagation loss that is intrinsic to the $Sc_{0.30}Al_{0.70}N$ based waveguide system because this measurement includes all sources off loss in the device.

Fabrication quality seems to play a significant role in the overall propagation losses, causing a substantial difference between the extrapolated values from the fit that considered all the devices and the values from only the fit that considered the best performing devices. In fact, fabrication quality seems to dominate the extracted value for the combined propagation loss in the bend and transitions. For most of the data, taking into account the simulated values of the transition losses, the estimated propagation losses in the bends are still much higher than the measured propagation losses in the straight portions. With a large bend radius (200 μm), and absent any

Optics EXPRESS

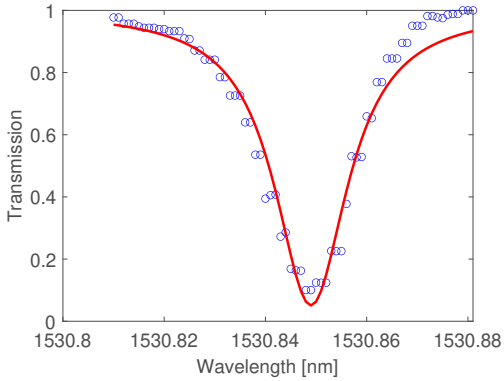

Fig. 6. Measured resonator response (blue) with fit (red). Q > 87000.

fabrication imperfections, the values are expected to be similar. Additionally, any trend that existed between film thickness and propagation loss in the bends was not identifiable, indicating that random variations in fabrication quality overshadowed underlying trends. On the other hand, the straight propagation losses showed a monotonic increase of loss per unit length with respect to film thickness. This indicates that while the propagation losses in the bends are dominated by a random feature of the device such as fabrication quality, the straight propagation losses are not, and instead originate from an effect of the film thickness variation. Furthermore, due to the etch depth being constant for all devices, any contribution of sidewall roughness to the straight propagation loss will decrease with film thickness. Instead, we see the opposite trend indicating that sidewall roughness is not the main source of straight propagation loss.

Altogether, the data suggests that the dominating factor of the straight propagation losses is the material absorption of the core material. Specifically, the $Sc_{0.30}Al_{0.70}N$ core must be more absorptive than the SiO_2 cladding because as the mode is pushed further into the core with a thicker film, the propagation loss increases. Although fabrication losses and or sidewall roughness do not dominate the straight propagation loss values, they may still play a role. The combination of all of the loss sources result in the relationship we see.

If we were to attribute all the straight propagation loss to material absorption in order to create an upper bound on the $Sc_{0.30}Al_{0.70}N$ absorption, the best approximation for the imaginary

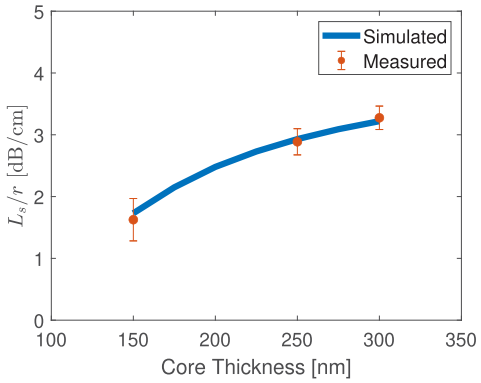

Fig. 7. Comparison of simulated and measured straight propagation loss. Extinction coefficient for $Sc_{0.30}Al_{0.70}N$ in simulation is 1e-5.

Optics EXPRESS

components of the refractive index, otherwise known as the extinction coefficients, of the material is 10^{-5}. Additionally, this approximation predicts, and does not assume, that the losses of the SiO_2 cladding layer are negligible ($<10^{-8}$). The closeness of the approximation can be assessed in Fig. 7. These values were determined by adjusting the extinction coefficients of the materials in 2D cross sectional simulations of the waveguides until the simulated trend of propagation losses across film thicknesses matched the trend extrapolated from the best performing devices.

5. Conclusions

In conclusion, we experimentally explored the optical propagation losses of $Sc_{0.30}Al_{0.70}N$ waveguides using their resonant behavior. We show the extracted propagation losses from the straight waveguides were dependent on the film thickness, mostly due to the material absorption, and are still low enough for many optical applications at a value of 1.6 ± 0.3 dB/cm. We suspect that propagation losses in the bending waveguides were up to 2 dB/cm higher than in the straight portions and highly dependent on the fabrication quality. These results allow for future studies of the ScAlN material platform, including more complex applications that take advantage of its unique properties such as acousto-optic and electro-optic modulators.

Funding. National Science Foundation (ECCS-1905834).

Disclosures. The authors declare no conflicts of interest.

Data availability. Data underlying the results presented in this paper are not publicly available at this time but may be obtained from the authors upon reasonable request.

References

1. C. Xiong, W. H. P. Pernice, and H. X. Tang, "Low-loss, silicon integrated, aluminum nitride photonic circuits and their use for electro-optic signal processing," Nano Lett. **12**(7), 3562–3568 (2012).
2. S. Liu, K. Xu, Q. Song, *et al.*, "Design of mid-infrared electro-optic modulators based on aluminum nitride waveguides," J. Lightwave Technol. **34**(16), 3837–3842 (2016).
3. S. Zhu and G.-Q. Lo, "Aluminum nitride electro-optic phase shifter for backend integration on silicon," Opt. Express **24**(12), 12501–12506 (2016).
4. K.-y. Hashimoto, S. Sato, A. Teshigahara, *et al.*, "High-performance surface acoustic wave resonators in the 1 to 3 ghz range using a scaln/6h-sic structure," IEEE Trans. Ultrason., Ferroelect., Freq. Contr. **60**(3), 637–642 (2013).
5. S. Fujii, M. Sumisaka, G. Tang, *et al.*, "Highly c-axis-oriented scaln thin films deposited using sc-al alloy target," (2015).
6. S. A. Tadesse and M. Li, "Sub-optical wavelength acoustic wave modulation of integrated photonic resonators at microwave frequencies," Nat. Commun. **5**(1), 5402 (2014).
7. H. Li, S. A. Tadesse, Q. Liu, *et al.*, "Nanophotonic cavity optomechanics with propagating acoustic waves at frequencies up to 12 ghz," Optica **2**(9), 826–831 (2015).
8. V. Yoshioka, J. Lu, Z. Tang, *et al.*, "Strongly enhanced second-order optical nonlinearity in CMOS-compatible Al1-xScxN thin films," APL Mater. **9**(10), 101104 (2021).
9. M. Baeumler, Y. Lu, N. Kurz, *et al.*, "Optical constants and band gap of wurtzite $Al_1 - xSc_xN/Al_2O_3$ prepared by magnetron sputter epitaxy for scandium concentrations up to x = 0.41," J. Appl. Phys. **126**(4), 045715 (2019).
10. S. Zhu, Q. Zhong, N. Li, *et al.*, "Integrated scaln photonic circuits on silicon substrate," in *Conference on Lasers and Electro-Optics* (Optica Publishing Group, 2020), paper STu3P.5.
11. J. Liu, A. Singh, P. Wang, *et al.*, "Quantum-relevant optical nonlinearity in aluminum nitride," in *CLEO 2023* (Optica Publishing Group, 2023), paper STu3N.4.
12. S. Barth, H. Bartzsch, D. Glöß, *et al.*, "Adjustment of plasma properties in magnetron sputtering by pulsed powering in unipolar/bipolar hybrid pulse mode," Surf. Coat. Technol. **290**, 73–76 (2016). Selected papers from the Society of Vacuum Coaters 58th Annual Technical Conference.
13. P. Frach, C. Gottfried, H. Bartzsch, *et al.*, "The double ring magnetron process module —a tool for stationary deposition of metals, insulators and reactive sputtered compounds," Surf. Coat. Technol. **90**(1-2), 75–81 (1997).
14. M. T. Hardy, B. P. Downey, D. J. Meyer, *et al.*, "Epitaxial scaln etch-stop layers grown by molecular beam epitaxy for selective etching of aln and gan," IEEE Trans. Semicond. Manufact. **30**(4), 475–479 (2017).
15. K. Airola, S. Mertin, J. Likonen, *et al.*, "High-fidelity patterning of aln and scaln thin films with wet chemical etching," Materialia **22**, 101403 (2022).